Geophysical Journal International

Geophys. J. Int. (2012) **191,** 1441–1456 doi: 10.1111/j.1365-246X.2012.05698.x

Crustal and uppermost mantle structure of southern Norway: results from surface wave analysis of ambient seismic noise and earthquake data

Andreas Köhler,[1] Christian Weidle[2] and Valérie Maupin[1]

[1] *Department of Geosciences, University of Oslo, P.O. Box 1047, 0316 Oslo, Norway. E-mail: andreas.kohler@geo.uio.no*
[2] *Institute of Geosciences, Christian-Albrechts-Universität zu Kiel, Kiel, Germany*

Accepted 2012 September 24. Received 2012 September 12; in original form 2012 March 2

SUMMARY

We use ambient seismic noise and earthquake recordings on a temporary regional network in southern Norway to produce Rayleigh and Love wave phase velocity maps from 3 to 67 s period. Local dispersion curves are then jointly inverted for a 3-D shear wave velocity model of the region. We perform a two-step inversion approach. First, a direct search, Monte Carlo algorithm is applied to find best fitting isotropic velocity depth profiles. Those profiles are then used as initial models for a linearised inversion which takes into account radial anisotropy in the shear wave structure. Results reveal crustal as well as uppermost mantle structures in the studied region. Velocity anomalies in the upper crust are rather small in amplitude and can in most parts be related to surface geology in terms of rock densities. Old tectonic units like the Oslo Graben (300–240 Ma) and the Caledonian nappes (440–410 Ma) are clearly imaged. Furthermore, we find clear indications for localized crustal anisotropy of about 3 per cent. Despite generally poor resolution of interface depths in surface wave inversion, we find lateral variation of crustal thickness in agreement with previous studies. We are able to confirm and locate the transition from a slow lithospheric upper mantle underneath southern Norway to a fast shield-like mantle towards Sweden.

Key words: Interferometry; Surface waves and free oscillations; Seismic anisotropy; Seismic tomography; Crustal structure.

GJI Seismology

1 INTRODUCTION

Using ambient seismic noise to estimate empirical Green's functions by cross-correlation has now become a well-established method in seismology (Shapiro & Campillo 2004; Sabra *et al.* 2005). This technique is of particular importance since it allows for inversion of shallow (i.e. crustal) structures based on surface waves, an approach which was previously limited by lack of earthquake surface wave observations in the period range between about 1 and 20 s. However, for longer periods beyond the spectral band of primary microseisms, the contribution from ambient seismic noise is decaying continuously and therefore limits depth resolution. A number of studies were published recently combining ambient seismic noise and earthquake analysis for inversion of local shear wave velocity depth profiles (e.g. Yao *et al.* 2008; Moschetti *et al.* 2010a; Yang *et al.* 2011). The benefit from this approach is a continuous sensitivity from shallow crustal to deeper mantle structures. Thus, fewer independent constraints such as Moho depth and crustal velocities are needed to image the upper mantle. Another advantage of short-period surface waves is the ability to analyse radial anisotropy in the crust in case of Rayleigh and Love wave observations (Moschetti *et al.* 2010b; Guo *et al.* 2012).

We present a 3-D *S*-wave velocity model of the crust and shallow upper mantle below southern Norway based on local measurements of Rayleigh and Love wave phase velocity dispersion curves inferred from ambient noise as well as teleseismic and regional earthquake records. Knowledge about the present depth structure in southern Norway is essential to improve our understanding of the so far unknown origin of the rather rough and high topography along the Scandes mountain range located at the edge of the Fennoscandian shield, far away from active plate boundaries. The discussion about source and timing of uplift is ongoing (Rohrman & van der Beek 1996; Japsen & Chalmers 2000; Lundin & Doré 2002; Nielsen *et al.* 2009; Chalmers *et al.* 2010) and will therefore benefit from new constraints such as present crustal thickness and upper mantle structure. This information will serve as a basis to develop new geodynamical models and will in particular help to evaluate the contribution of mantle processes as sources for the uplift.

The structure in southern Norway has been recently analysed using body wave tomography (Medhus *et al.* 2012; Wawerzinek *et al.* 2012), seismic receiver functions (Frassetto, in preparation), active seismic source refraction (Stratford & Thybo 2011), and gravity modelling (Ebbing & Olesen 2005; Ebbing *et al.* 2012). Earthquake generated surface waves have so far been used for a regional

3-D model of northern Europe (Weidle & Maupin 2008), with limited resolution in southern Norway, and for an average (1-D) shear wave model for southern Norway (Maupin 2011). Furthermore, a group velocity tomography based on ambient seismic noise, not including depth inversions, has been carried out (Köhler *et al.* 2011). A consistent result in those studies is a significant difference in upper mantle seismic velocities in southern Norway compared to bordering regions to the East (Maupin 2011; Medhus *et al.* 2012).

This work is a follow-up of Köhler *et al.* (2011) and Maupin (2011). The ambient noise data used to calculate the Rayleigh wave group velocity maps in Köhler *et al.* (2011) are used here to calculate Rayleigh wave phase velocity maps. The frequency range is widened by combining these maps with phase velocity maps from earthquake surface wave data. The area under study is also extended to the East by using data from six additional stations located in Sweden. The transverse components of the noise and earthquake data are used to obtain also Love wave phase velocity maps. Finally, depth inversion is performed that yields a 3-D model of SV-wave velocities and radial anisotropy.

In Section 2 we describe the methods used to calculate phase velocity maps from ambient noise and earthquake records. We then present our method to invert for the 3-D shear wave model, which is a combination of a Monte Carlo and a linear inversion technique. Finally, we present and discuss our results and relate them to previous findings and existing models in southern Norway in Sections 4 and 5, addressing crustal structure and Moho depth, uppermost mantle velocities, and radial anisotropy.

2 PHASE VELOCITY MAPS

Phase velocity maps are produced in the period range 3 to 67 s for Rayleigh waves and 4 and 50 s for Love waves using both ambient seismic noise and earthquake data. Phase velocity maps are generated from both data sets separately with different procedures that will be described below, and then combined in local dispersion curves.

The total studied area comprises southern Norway and part of southern Sweden, combining data from 41 seismic broadband receivers of the MAGNUS network (Weidle *et al.* 2010) to the West with data from six temporary stations in Sweden (DANSEIS, Fig. 1) to the East. The MAGNUS stations were recording between September 2006 and June 2008 while data from DANSEIS stations is available from April 2008, corresponding to an overlap of only 3 months. We can only use data recorded simultaneously at all stations in case of earthquake data since 2-D phase (velocity) maps are interpolated directly from the phase measurements at all receivers. Therefore, only data recorded between April and June 2008 are used which limits a bit the quality of the results we can obtain from the earthquake data. For ambient noise, since inter-station phase velocities can be measured as soon as two stations record simultaneously, we use the complete record of 20 months for stations pairs including MAGNUS stations only and 3 months for those including DANSEIS stations. We found the period of 3 months to be sufficient to obtain good velocity data from seismic noise.

2.1 Ambient seismic noise

2.1.1 Processing

We follow Bensen *et al.* (2007) for data preprocessing, cross-correlation of ambient seismic noise, and stacking of noise cross-correlation functions (NCFs). After preprocessing (instrument correction, bandpass filtering, time domain normalization by a running absolute mean, pre-whitening of spectrum in frequency domain), we compute cross-spectra for each station pair using the vertical and tangential seismogram component of 15-min long time windows. We transform the cross-spectra back into time domain and stack them over time intervals of 3 months duration with 1 month overlap. In addition a stack over 20 months is prepared. More details are described in Köhler *et al.* (2011) where a group velocity tomography of the studied area is presented. In that study, also detailed investigations on the directionality of the ambient noise wavefield in southern Norway were made and the reliability of empirical Green's function estimates was shown.

Here, we measure phase velocity dispersion curves for each station pair and for each of the 18 three-months long noise cross-correlation stacks of the vertical and transverse wavefield component by applying time frequency analysis (FTAN, Levshin *et al.* 1989; Ritzwoller & Levshin 1998). We determine velocities separately from the causal and acausal component of the NCFs and apply FTAN interactively which helps us to select only reasonable dispersion curves (Köhler *et al.* 2011). Since separation

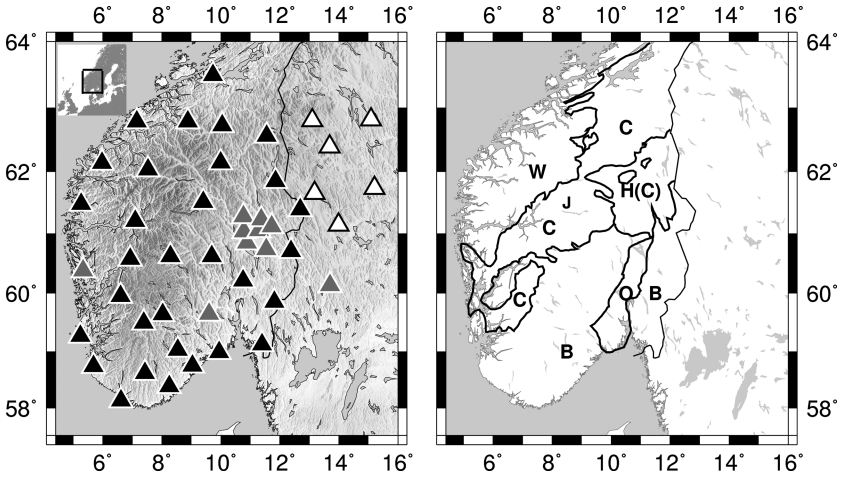

Figure 1. Studied area in southern Norway. Left panel: Black triangles indicate temporary and grey permanent broadband stations of MAGNUS seismic network. White symbols show temporary DANSEIS network in Sweden. Right panel: Outline of main geological unit: Fennoscandian Basement (B), Caledonian nappes (C) including Jotun nappes (J) and Hedmark group (H), Oslo Graben (O) and Western Gneiss Region (W).

between fundamental and higher modes is good in the considered period band for phase velocities, we ensure that only the fundamental mode dispersion curve is measured for Rayleigh and Love waves. An averaged dispersion curve and its standard deviation is computed for both wave types for each path from all measurements on the individual 3-months stacks. For station pairs including DANSEIS stations, only a single NCF stack can be processed. We are able to measure Rayleigh wave phase velocities from 3 to 30 and Love wave phase velocities between 4 and 14 s period (see Supporting Information Figs S1 and S2). The more limited period range for Love waves is probably due to their smaller energy contribution to the microseismic wavefield, which is dominated by Rayleigh waves (Lacoss *et al.* 1969).

2.1.2 Phase velocity tomography

The careful data selection procedure for the tomographical inversion of group velocity measurements used in Köhler *et al.* (2011) is applied for the phase velocities. We use selection criteria for each station pair assessing the signal to noise ratios (SNR) of NCFs, the number of useful 3-months stacks (i.e. those we were able to pick dispersion curves from in FTAN), and the standard deviation of velocity measurements (computed from measurements on all 3-month stacks). The broadband SNR must be higher than 12 for each 3-month stack. Furthermore, for the 20-month stack SNRs are required to be higher than 15 for the broadband signal as well as for the NCFs filtered at each target period used for the tomography. Finally, the phase velocity measurements at each period must satisfy the requirement that the number of useful 3-month stacks is higher than three, the wavelength is shorter than one-third of the interstation distance, and the standard deviation of phase velocity is lower than 0.05 km s^{-1}.

Due to lack of data, we cannot provide a phase velocity standard deviation for station pairs including DANSEIS stations. Therefore, quality control for those data is restricted to the SNR and wavelength criterion and we cannot avoid to introduce some potential uncertainty. However, the SNR has been shown to be a very robust selection criterion in many ambient noise studies. Furthermore, we tested lower weights for station pairs including DANSEIS stations in the tomography and found no significant effect on the phase velocity maps. We are therefore confident that the smaller amount of data does not bias our results in the Northeast.

We invert for Rayleigh and Love wave phase velocity maps using the common tomographic inversion method of Barmin *et al.* (2001) using the same inversion parameters as in Köhler *et al.* (2011). A 0.2×0.2 degree grid and a starting model corresponding to the averaged observed velocity at each period is used. The regularization parameters used are $\alpha = 400$ (weight) and $\sigma = 40$ km (correlation length). Please see Barmin *et al.* (2001) for details. The rms, i.e. the difference between input data (measured velocity for each station pair) and initial velocity (constant starting model), is reduced by 50 per cent maximum at 3 s and 10 per cent minimum at 30 s period after inversion. The low number at long periods can be explained by a rather small lateral variation of phase velocities in the studied area. Figs 2(a)–(c) show a selection of phase velocity maps after resampling on a 0.25×0.125 degree grid.

The phase velocity maps shown here are in agreement with the group velocity maps in Köhler *et al.* (2011). We observe clear velocity anomalies for Rayleigh and Love waves of about ± 3 per cent at short and long periods showing correlations with geological structures as discussed in case of the group velocity tomography. The dashed contour lines in Figs 2(a)–(c) indicate a resolution estimate based on the method of Barmin *et al.* (2001). A contour line can be plotted for a specific value in km. All inverted anomalies having extends larger than this value inside the contour are reliable observations. Here, we choose a value of 23 km to show the reliability of all inverted anomalies which have diameters not smaller than about 50 km. For a full resolution analysis including paths densities and a checkerboard test for the MAGNUS network we refer to Köhler *et al.* (2011).

The western parts of southern Norway are dominated by a rough topography. The depth sensitivity of our Rayleigh waves at 3 s is about 3 km which is comparable to the altitude variations which can be as large as 2.5 km on a very short horizontal distance (less than 10 km). Since rough topography could possibly bias phase velocities at short seismic wavelengths, we therefore investigated whether the low velocities found in this region could be an artifact of the propagation (Köhler *et al.* 2012). Using synthetic data generated by spectral elements modelling, it was shown that the measurable impact is too small to explain the amplitudes of velocity anomalies observed here. An empirical linear regression model which relates the phase velocity bias to the averaged absolute value of the topographic gradient within a radius of 15 km from the measurement site (1 km sampling) suggests that the impact of topography does not exceed -0.5 per cent at 3 s period for the receivers considered here. For most receivers and at longer periods it is below significance (-0.2 per cent on average). We therefore conclude that low phase velocities observed at short periods in the western part of southern Norway can safely be interpreted as the result of low *S*-wave velocities in the upper crust.

2.2 Earthquake data

2.2.1 Phase measurements

The phases were measured on the individual seismograms using the vertical components for the Rayleigh waves and the transverse components for the Love waves. Time windows and data selection follow broadly the procedure described in Maupin (2011) to select data for beamforming analysis, but with some modifications to further reject individual noisy data that could bias the phase interpolation procedure used to generate phase velocity maps. The main difference with Maupin (2011) is that the data are corrected by an average moveout of 0.25 s km^{-1} before processing in order to be able to sharpen the selection criteria based on envelope comparisons: for a given event and frequency, individual records whose envelope differed from the mean one by more than 0.75 times the maximum of the mean envelope were rejected, as well as all records if the ratio between the average and maximum amplitude of the mean envelope was lower than 6.0 (5.0 for Love waves). Furthermore, a larger geographical area is analysed due to the inclusion of the DANSEIS stations in addition to the MAGNUS network. This is at the expense of the time period for which data are available, as discussed earlier, reducing the recording period from almost 2 yr to only 3 months.

The data set consists of 35 events, 21 teleseismic events with epicentral distances between 47 and 100 degrees and magnitude of at least 6.0, and 14 regional events with epicentral distances varying from 13 to 30 degrees and magnitudes of at least 5.1. In all cases, we selected events with focal depths not larger than 100 km, ensuring dominant surface wave fundamental modes. The inclusion of regional as well teleseismic events assures that we have

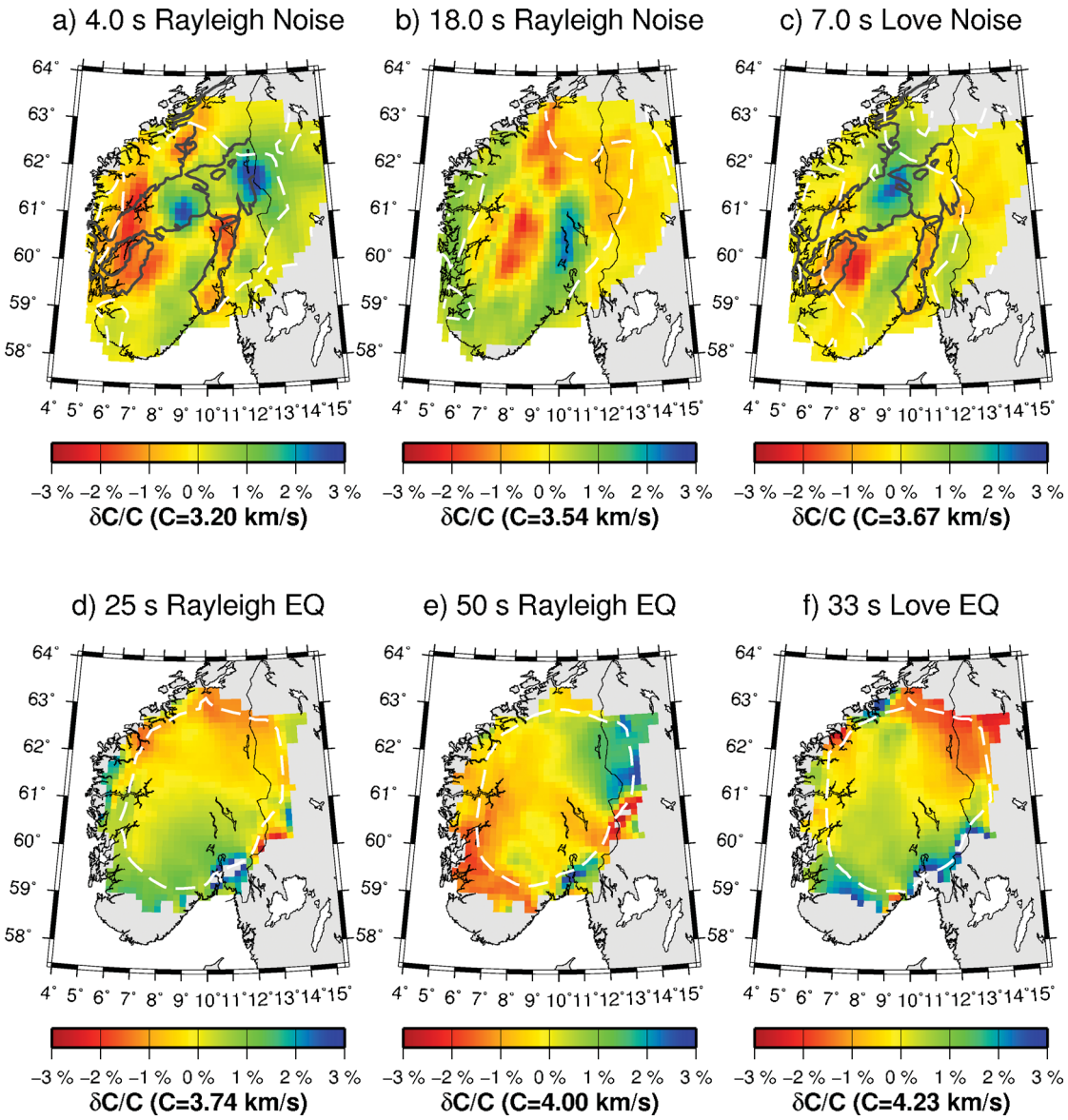

Figure 2. Rayleigh and Love wave phase velocity maps at selected periods obtained by ambient seismic noise tomography (a–c) and phase interpolation of earthquake observations (d–f). Lines in (a) and (c): Outline of geological units (see Fig. 1). White dashed lines indicate resolution limits: 23 km contour based on method of Barmin *et al.* (2001) in (a)–(c) and relative sampling contour of three (number of velocity estimates by number of nodes) in (d)–(f).

an adequate azimuthal distribution of data despite the short period of 3 months for which we could analyse data (Table 1).

2.2.2 *Phase interpolation*

Analysis of the measured phases follows the interpolation-based method by Weidle (2012) which we briefly summarize in the following. First, to homogenize the data distribution, three of the seven broadband stations of the dense NORSAR array are omitted. Additionally, events with less than 12 observations are discarded.

A crucial step in the preprocessing to the interpolation is unwrapping of the periodic phase measurement to an absolute phase. Since we want to account for possible deviations of the propagation direction of the wavefield from the great-circle path, we try to avoid enforced phase alignment transverse to the great-circle direction. We do this, for each event separately, by splitting the available observations into subsets of $\geq$9 stations after sorting the station list by azimuth. Each of these subsets is then unwrapped taking into account the epicentral distance and a reference velocity. Based on the interstation distance of two neighbouring stations in the subset, we compare the measured phase difference with an expected difference from the reference velocity and add or subtract 2π to/from the measurement if the difference in the measured and expected phase difference exceeds π. The reference velocity is taken from Maupin (2011), however, we found that the unwrapping is not very sensitive to the chosen reference. This may be different though in other regions with significant velocity anomalies.

In a last step, the unwrapped phases in the different subsets need to be aligned to a common reference which we chose as a 'central' epicentral distance which is common to all subsets. The unwrapped phase at the stations closest to this 'central' distance in each of the subsets is compared, and, if the phase difference between them

Table 1. List of events used as earthquake data. 'R' stands for regional and 'T' for teleseismic events. Distance (Dist) is given in degrees, BAZ is backazimuth, and Mw is moment magnitude.

Type	Date	Time	Lat	Lon	Dist	BAZ	*M*w	Region
R	28 March 2008	00:16:19.90	34.758	25.345	28.129	149.19	5.6	Crete, Greece
R	10 May 2008	20:53:04.20	36.300	22.240	25.922	153.55	5.4	Southern Greece
R	24 May 2008	04:58:18.87	42.386	−30.515	29.657	249.78	5.5	Azores Islands Region
R	28 May 2008	13:19:52.67	84.912	12.899	24.445	0.99	5.2	North of Svalbard
R	06 June 2008	20:02:56.89	35.883	−0.658	25.412	197.12	5.5	Northern Algeria
R	08 June 2008	12:25:29.71	37.963	21.525	24.169	153.77	6.3	Southern Greece
R	12 December 2008	00:20:45.60	35.110	26.190	28.014	147.56	5.2	Crete, Greece
T	15 April 2008	03:03:04.66	13.564	−90.599	82.610	284.34	6.1	Near Coast of Guatemala
T	24 April 2008	12:14:49.92	−1.182	−23.471	66.335	215.07	6.5	Central Mid-atlantic Ridge
T	07 May 2008	16:45:18.70	36.164	141.526	76.247	37.37	6.9	Near East Coast of Honshu
T	09 May 2008	21:51:29.73	12.516	143.181	98.775	44.43	6.8	South of Mariana Islands
T	12 May 2008	06:28:01.57	31.002	103.322	65.875	69.59	7.9	Sichuan, China
T	12 May 2008	11:11:02.48	31.214	103.618	65.834	69.23	6.1	Sichuan, China
T	23 May 2008	19:35:34.78	7.313	−34.897	62.181	230.14	6.5	Central Mid-atlantic Ridge
T	25 May 2008	08:21:49.99	32.560	105.423	65.528	67.02	6.1	Sichuan, China
T	25 May 2008	19:18:25.71	56.087	−153.780	62.778	348.81	6.0	Kodiak Island Region
T	01 June 2008	01:57:24.33	20.127	121.370	83.343	60.5	6.3	Philippine Islands Region
T	13 June 2008	23:43:45.36	39.030	140.881	73.402	36.75	6.9	Eastern Honshu, Japan

exceeds $1.1 \cdot \pi$, 2π is added or subtracted to all stations in one of the subsets.

After phase unwrapping, the phases are interpolated for each event and at each period separately with the multiscale interpolation scheme by Weidle (2012). In this regularization-free approach, a multitude of phase interpolations is calculated for many subsets of the available data. For each of these subsets, the region is triangulated as constrained by the observation points and the phases between these points bilinearly interpolated. This yields, for each event, a multitude of coarse, low-resolution phase velocity maps which are consequently averaged to return one phase velocity map of the network region per event, including a statistical estimate of the standard deviation in phase velocity at each interpolation point.

By weighted averaging of several such single-event phase velocity maps, Weidle (2012) has shown that reliable estimates on isotropic phase velocity within the network region can be derived from as few as four observed wavefields. Since this approach involves no *a priori* estimate on data covariance, large data uncertainties (e.g. measurement or unwrapping errors) may propagate in the interpolated maps while minor uncertainties are amended by the multiscale approach. It is thus necessary to manually discard wavefields which could not be reconstructed to a subplanar wavefield. This manual selection resulted in 18 remaining events overall which are listed in Table 1, where a number of 6–10 events are used for Rayleigh waves at periods between 25 and 67 s, and 4–6 events for Love waves between 18 and 50 s period.

Figs 2(d)–(f) shows some examples of resulting phase velocity maps. As no regularisation is applied, remaining artifacts from data uncertainties are still prevalent towards the bounds of the network region. We use a relative sampling parameter S as the ratio of the number of velocity estimates per interpolation point to the number of actual stations from which these velocity estimates are derived (Weidle 2012). For values $S > 3$ we assume that the phase velocity estimates should be largely free of artifacts.

The increase in crustal thickness from southwest to northeast is nicely seen for Rayleigh waves at 25 s and for Love waves at 33 s with a velocity contrast of around 2–3 per cent. At 50 s the contrast changes polarity, as the eastern part of the network region appears to be significantly faster than most of southern Norway. The contrast of around 4 per cent agrees roughly with observations from body waves which image a transition to faster velocities in southeastern Norway (Medhus *et al.* 2012; Wawerzinek *et al.* 2012).

Since only relatively few events were left for analysis due to the short time overlap between MAGNUS and DANSEIS stations, we thoroughly compared the results with results based on data from the MAGNUS network only (20 months of data, see Supporting Information Fig. S3 online). The maps from MAGNUS data return the same average velocity in the network region and very similar trends in the distribution of phase velocity deviations as the maps presented here. Due to the smaller network region of the MAGNUS only data set, the contrasting velocities from west to east are, however, less clearly imaged.

3 INVERSION OF LOCAL DISPERSION CURVES

We then combine the Rayleigh and Love wave phase velocity dispersion curves from ambient seismic noise tomography and earthquake phase interpolation in order to perform a joint inversion. The dispersion data comprises Rayleigh waves from 3 to 30 s for ambient noise and 25 to 67 s for earthquake data. In the overlapping period band, ambient noise phase velocities are sampled at 25 and 30 s and earthquake data at 25, 28.6 and 33.3 s. We average at 25 s and use the remaining sampling periods independently. Fig. 4 shows that dispersion data obtained from ambient noise and earthquakes are consistent in the overlapping period band. The difference at 25 s was found to be smaller than 0.05 km s^{-1} and of the same order as the measurement uncertainty of the individual methods. Phase velocity measurements for Love waves are used between 4 and 14 s for noise and 18 and 50 s for earthquakes.

We invert for local velocity depth profiles on a 0.5 × 0.25 degree grid. In a first inversion step (in the following referred to as Inversion I), we use the Neighbourhood Algorithm of Sambridge (1999), adapted and implemented to find isotropic, layered models fitting dispersion data (Wathelet *et al.* 2004; Wathelet 2008). Due to discrepancy between Rayleigh and Love waves (see below), a second inversion run is conducted using a linearised inversion which

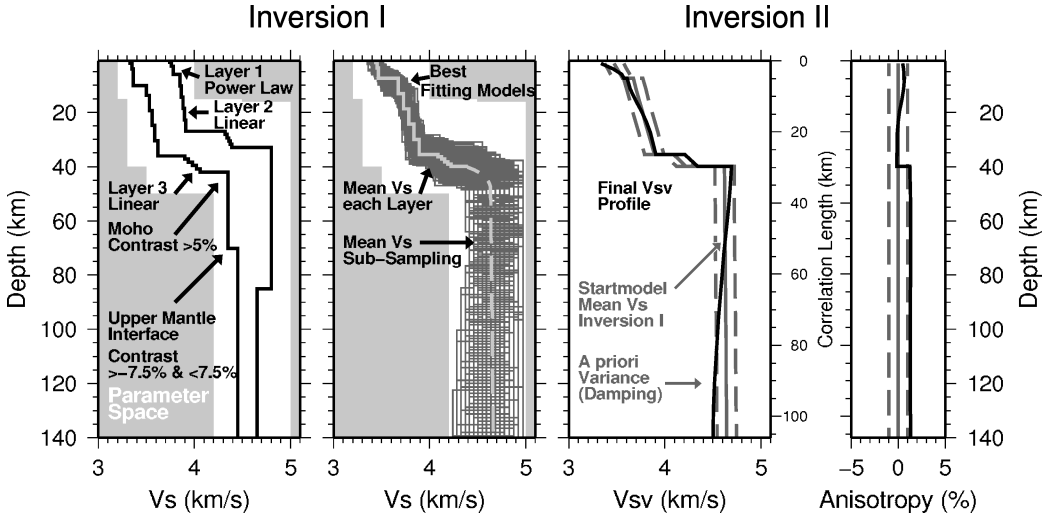

Figure 3. Schematic description of inversion procedure. In Inversion I an iterative Monte Carlo sampling of the model space is performed. First panel shows two examples of generated models within allowed range of model parameters. Range and constraints on model parameters are given. 'Linear' and 'Power Law' refers to manner of velocity increase within layer. Ensemble of best fitting models is used to compute a starting model for Inversion II (see text). Inversion II includes radial anisotropy. *A priori* model variance (damping) is indicated by grey dashed lines and starting models by solid grey lines for both model parameters (V_{SV} and anisotropy). Note that two different scales are used for Y-axis in Inversion II plots. Correlation length with depth in Inversion II (see text) is represented by ticks of one Y-axis and depth is used for the other. Examples profiles shown in both inversion steps correspond to inversion of an average dispersion curve for the entire study area.

Table 2. Ranges for model parameters in Inversion I. Note that Layer 3 is parameterised by a range for thickness and not bottom depth. 'V in layer' refers to depth distribution of velocity within a layer, accomplished through five sub-layers. Density is uniform within each layer. Poisson ratio is limited between 0.2 and 0.5.

	Bottom depth (km)	V_S (km s^{-1})	V_P (km s^{-1})	V in layer	Density (g ccm^{-1})
Layer 1	1–15	3.2–4.0	3.0–7.0	Power law	2.0–3.7
Layer 2	15–40	3.3–4.0	4.0–8.0	Linear increase	2.2–3.7
Layer 3	1–10 (thickness)	3.5–4.5	4.0–8.0	Linear increase	2.2–3.7
Layer 4	50–150	4.2–5.0	5.0–9.0	Uniform	2.5–4.0
Halfspace	–	4.2–5.0	5.0–9.0	Uniform	2.5–4.0

takes into account radial anisotropy and adjusts the V_{SV} structure accordingly without changing interface depths (Inversion II).

3.1 Inversion I

Before we perform Inversion I, an empirical spherical correction is applied to the velocity measurements since the implementation we use has originally been developed to invert shallow models in a flat-earth setting. In order to find the correction, we generated random velocity models in the parameterised model space described in the next paragraphs. For each model two dispersion curves were forward computed using a flat and a spherical earth model. We then found the correction for each period by linear regression. Potential errors obtained through this simple approach are implicitly corrected later in Inversion II which assumes a spherical earth model.

The Neighbourhood Algorithm is a derivative-free, direct search algorithm which performs an iterative Monte Carlo sampling of the model space. The goal is to find an ensemble of models fitting the data, rather than a single optimal solution. The parameterisation, constraints, and *a priori* assumptions are summarised in Fig. 3 and Table 2. We invert for V_S, V_P, density, and interface depths.

We tested different parameterisations and found three layers for the crust and one layer over halfspace for the upper mantle to be optimal. We use a rather permissive parameterisation allowing for moderate to large variations of interface depths and medium parameters within realistic physical bounds (see Table 2 and Fig. 3a). The range for V_P/V_S is constrained through limits for the Poisson ratio (0.2–0.5). Within each crustal layer, velocities are allowed to increase with depth through a subset of five homogeneous sublayers, each with a constant velocity. Velocities of sublayers are constrained to an overall linear increase with sublayer and depth (Layer 2 and 3) or to a power-law increase (Layer 1) (Wathelet *et al.* 2004). Densities are uniform in each layer. The third layer is limited to a maximum thickness of 10 km and is meant to account for a possible fast lower-crustal body as reported for the eastern part of southern Norway (Pascal *et al.* 2007; Stratford & Thybo 2011). In order to assure that the upper three layers represent the crust, we claim a minimum velocity contrast of 5 per cent for V_S at the Moho interface (Layer 3–Layer 4). Layer 4 is introduced to take into account arbitrary, gradual velocity changes in the upper mantle (increase and decrease). We tried to use a linear or power-law velocity variation as for the crust, but found it more useful to invert with a single layer with constant velocity over halfspace. The velocity contrast at the mantle interface (Layer 4 – halfspace) is limited to $\pm$7.5 per cent. A continuous velocity-depth distribution, which is an appropriate initial model for Inversion II, is obtained by averaging all best fitting profiles in the mantle as described later.

An initial number of 100 models is generated and the 50 best Voronoi cells in the model space (see Sambridge 1999) are chosen to generate 100 new models in each iteration. We stop the inversion after 250 iterations. A number of 5 inversion runs is carried

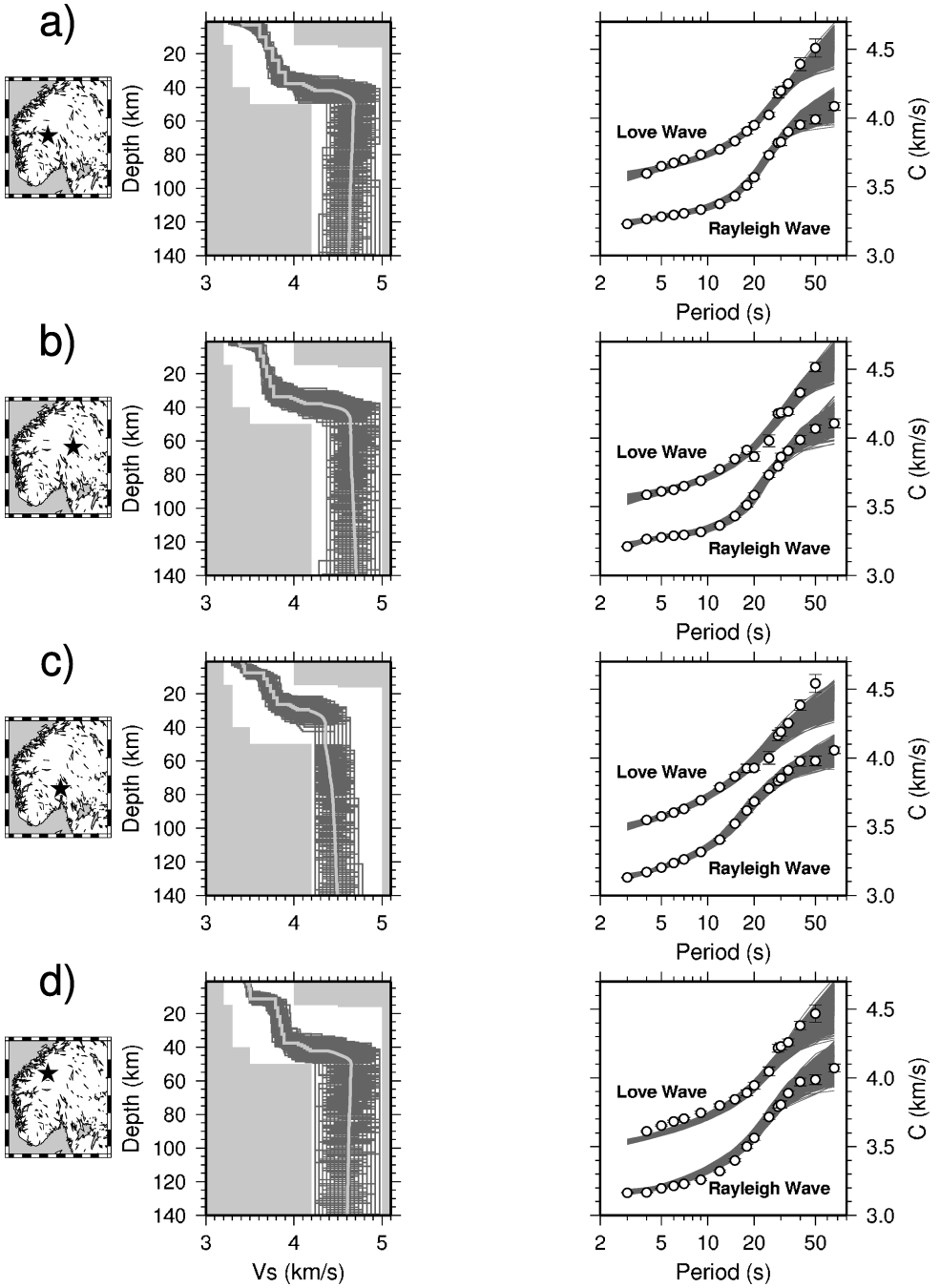

Figure 4. Representative examples of inverted models, Inversion I: Star in leftmost panel indicates location. Dark grey V_S profiles are ensemble of best fitting models. Light grey profile is corresponding averaged model. Rightmost panels: Symbols show measured phase velocities, grey lines dispersion curves of best fitting models.

out, each with a different random seed which controls the initially generated set of models. The model misfit (Chi-Squared statistic) is computed as:

$$\chi^2 = \frac{1}{N}\sum_{i=1}^{N}\frac{\left(d_i^s - p_i\right)^2}{\sigma_i^2}, \tag{1}$$

where N is the number of data samples, d_i^s are the observed, spherical-corrected phase velocities for Rayleigh and Love waves, p_i are the phase velocities forward computed from the model, and σ_i is the data standard deviation. The latter one is the uncertainty obtained from the phase velocity measurements on different NCFs stacks or from the phase interpolation method at longer periods (see above). For ambient noise, the standard deviation of velocity data obtained from MAGNUS stations does not vary significantly over the studied area (after data selection for tomography). We therefore compute the mean uncertainty at each period and assign the corresponding value to each grid point, including those covered by DANSEIS stations.

According to eq. (1), all models fitting the data within their uncertainties should have a misfit value lower than one. Theoretically, it is therefore advisable to use this value as misift threshold for selecting the best-fitting models. However, due to some scatter of data at longer periods (see Fig. 4), too few models are found below

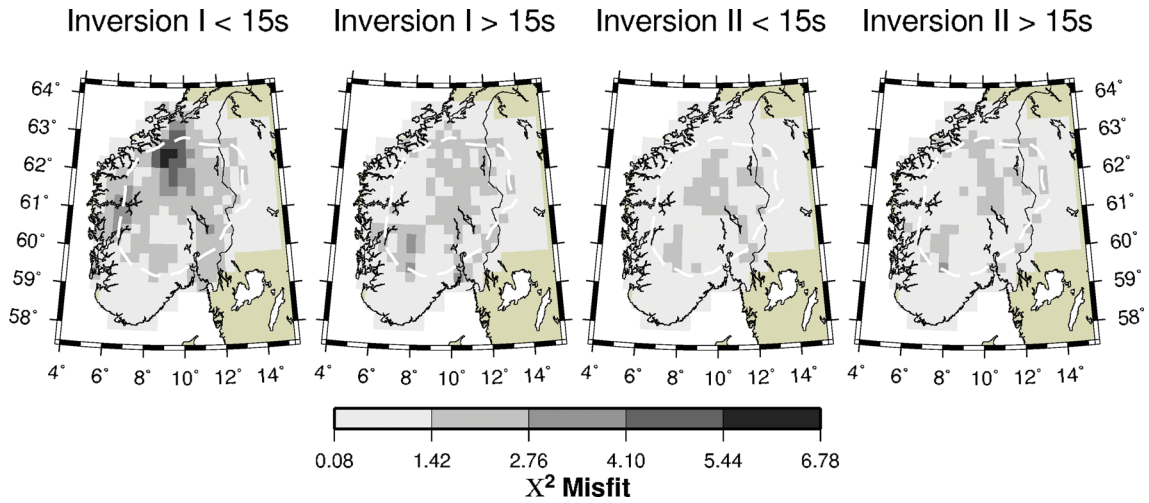

Figure 5. Minimum misfit in ensemble of best-fitting models at each grid location after Inversion I and final misfit after Inversion II. Misfit is computed in two period bands separately (3–15 and 15–67 s). White dashed lines indicates resolution limit according to phase interpolation method. Outside contour, only phase velocity measurements from ambient noise are used for inversion.

this threshold. We therefore start with a maximum misfit of 1.5 and increase it incrementally by 0.1 if less than 1000 models are found at each location for all five inversion runs. A number of 1000 models is an appropriate value to obtain a reliable statistic for model averaging. The corresponding minimum misfit in the ensemble of best fitting models at each location in Fig. 5 and an average maximum misfit of $\chi^2 = 2.3$ show that a majority of models explains the data well.

Fig. 4 shows the results of the inversion at four different locations. For the three first ones (Figs 4a–c), we observe a good fit between the measured and predicted dispersion curves. For the last one, we observe that the predicted velocities are too high for Rayleigh waves and too low for Love waves. This Love-Rayleigh discrepancy shows that no isotropic model satisfying simultaneously the dispersions of both wave types could be found, and is usually considered as an indication for the presence of radial anisotropy.

The example in Fig. 4(d) is typical for the region in the northwest area (8–10 degree E, 61.5–63 degree N) in the first panel of Fig. 5, where we observe regions of large misfits at short periods. In order to reduce this misfit, we therefore perform a second inversion that adjusts the models taking into account the presence of radial anisotropy.

3.2 Inversion II

Inversion II is a linear inversion that adjusts the *S*-wave velocities found by Inversion I into the *SV*-wave velocity and the depth-dependent anisotropy parameter $\xi = (V_{\rm SH}/V_{\rm SV})^2$. The depth of the interfaces are kept fixed during inversion. A linear inversion is adequate here and much more efficient than a new Neighborhood Algorithm search as in Inversion I since we already have obtained a good starting model, an element that favours the use of a linear inversion.

The starting model is obtained by averaging the ensemble of best fitting models from Inversion I. If the individual layer interfaces are found at comparable depths for all models inverted at one particular location (i.e. a single global misfit minimum for depth parameter), the average model can be obtained by computing mean velocity and interface depths of each sublayer. Results show that this approach is appropriate for most crustal model ensembles. However, when the inversion does not find a well-constrained interface, as it is the case in the upper mantle between Layer 4 and the halfspace, it is more useful to subsample all models every kilometre with depth and compute a continuous, average velocity profile without keeping the location of interface depths. Hence, the initial model for Inversion II is a combination of both model averaging techniques. The first approach is used for the crust and the Moho and the second for the upper mantle (see Fig. 3).

It is well known that interface depths are not well resolved by surface wave inversion. Since we will use fixed interface depths in Inversion II, we need to ensure that they are not biased by radial anisotropy in Inversion I. This is of particular importance for the Moho depth which we focus on in the model interpretation. Therefore, we perform a second inversion run of Inversion I without using Love waves at longer periods (>14 s) and compare the inverted Moho depths of the averaged models. Results show that the difference between Moho depths obtained by both inversion runs clearly follows a normal distribution with zero mean. Hence, there is no systematic bias of Moho depths for the majority of locations. However, we find a few outliers corresponding mainly to a region of clear Rayleigh-Love wave discrepancy at periods corresponding to lower crustal depth sensitivity (7–8 degree E, 59.75–60.75 degree N). For all locations having a difference in Moho depth of more than 5 km, we therefore use as initial model for Inversion II the averaged model of Inversion I without long-period Love wave data. Without those outliers (i.e. only data with Moho difference $\leq$5 km), we obtain a standard deviation for the Moho difference of 1.4 km which may partly indicate the depth resolution, but also includes the effect of using less data in the second run of Inversion I. A better estimate for the Moho depth uncertainty is given later.

We conduct Inversion II using the fundamental formula for a simple linear case following Tarantola & Valette (1982):

$$\vec{m} - \vec{m}_0 = \left(G^T\, C_{dd}^{-1}\, G + C_{mm}^{-1}\right)^{-1}\, G^T\, C_{dd}^{-1}(\vec{d} - \vec{d}_0), \qquad (2)$$

where $\vec{m}$ is the inverted model, $\vec{m}_0$ is the starting model from Inversion I, $\vec{d}$ are the measured phase velocities and C_{dd} their covariance matrix (based on data standard deviation previously used in Inversion I). Both $\vec{d}_0$, the phase velocities in the initial model, and G, the matrix of partial derivatives with respect to the model parameters, were calculated using a program from Saito (1988). We only invert for $V_{\rm SV}$ and ξ. The other parameters, $V_{\rm P}$ and densities, as well as

the crustal interface depths are kept fixed as given by the starting model. The model parameters we invert for are represented by a continuous function sampled at different depth points within each layer. The smoothness of the model variations with depth is controlled by an *a priori* correlation function that partly couples the variations of the parameter with depth through non-diagonal terms in the model *a priori* covariance matrix C_{mm}. We use Gaussian correlation functions and vary correlation length with depth (Maupin 2011). The *a priori* covariance between the model parameters at two depth-points z_1 and z_2 is then expressed as:

$$C_{mm}(m(z_1), m(z_2)) = \sigma_m^2 \exp(-(z_1 - z_2)^2/(2L(z_M)^2)) \quad (3)$$

where the correlation length L is a chosen function of z_M, the midpoint between z_1 and z_2, and σ_m is the *a priori* standard deviation of the model parameters. We choose σ_m to be 0.1 km s^{-1} for V_{SV} and 0.02 for ξ, and L to increase linearly from 1 km at the surface to 150 km at 200 km depth (see Fig. 3). Velocity variations across boundaries are decoupled. Since we use a continuous velocity structure for the upper mantle, we have one interface less than in Inversion I (two within the crust and the Moho). Finally, we evaluate the inverted depth distribution of V_{SV} and ξ at each location visually and increase the damping (i.e. decrease of σ_m to 0.05 km s^{-1}) if necessary to avoid unrealistic oscillation of model parameters.

Taking into account radial anisotropy reduces the misfit considerably at short periods and also slightly at longer periods as shown in Figs 5 and 6. The latter figure presents results of Inversion II for the same locations as in Fig. 4. Results for location in Fig. 6(d) show that the inverted model explains both Rayleigh and Love wave velocities, whereas for the other locations anisotropy in the crust is low and velocity is changed only slightly at upper mantle depths (Figs 6a–c).

4 RESULTS

4.1 Three-dimensional shear wave structure

Figs 7(a)–(e) show the results of the inversion in terms of maps of average *SV* wave velocities in different depth ranges. Note that no lateral smoothing is done at this stage. Furthermore, we show the velocity structure along two cross-sections in Figs 7(g)–(h) after smoothing the results laterally by averaging in 1 × 0.5 degree cells and resampling at a rate of 0.25 degrees. At shallow depths of about 5 km, lateral velocity variations partially correlate well with surface geology. The Oslo Graben is characterised by lower velocity of about 3.45 km s^{-1}, whereas higher velocities of about 3.6 km s^{-1} are found to the northeast and northwest, the latter one being related to the Jotun nappes of the Caledonides. The uppermost crust of the western part of southern Norway seems to be generally slower than further East. Similar trends can be observed in the lower part of the upper crust at depths of about 10 km. However, within the upper part of the lower crust (about 20 km depth), the Oslo Graben and the northwesternmost region close to the coast are characterised by slightly higher velocities of up to 3.85 km s^{-1} compared to the remaining areas with about 3.7 to 3.75 km s^{-1}.

The interface between Layer 3 and the halfspace varies relatively smoothly between depths of about 30 to 44 km. This gives the Moho map shown in Fig. 7(f). There is a general trend of increasing crustal thickness from Southwest to Northeast and a clearly shallower Moho in parts of the Oslo Graben. It seems from Fig. 7(d) that sub-Moho velocities are partially correlated with variations in crustal thickness in the South. We will discuss this possible trade-off in the next section. In the upper mantle at depth of about 100 km (Fig. 7e), we observe a clear trend towards higher velocities from about 4.45 km s^{-1} in the West to 4.65 km s^{-1} in the East.

4.2 Model resolution and trade-offs

The *posteriori* standard deviation of V_{SV} is shown in Fig. 8(a) averaged over two depth ranges. Note that the uncertainty is lower at those locations where we had to use a stronger damping in order to avoid oscillation of model parameters (see rightmost panel in Fig. 8a). The model uncertainty is not larger than about 0.03 km s^{-1} in the crust and 0.05 km s^{-1} in the upper mantle. Hence, the general trends described above seem to be significant patterns, however the spread in velocity at adjoining locations on a smaller scale is partly below the model resolution. From Inversion I we obtain standard errors for Moho depths by averaging the ensemble of best fitting models at each location as described above. An average value of about 500 m is obtained. The general trend in crustal thickness described above is therefore a reliable observation.

We also invert data computed from a synthetic velocity model to test the effect of model parametrization and averaging in our two-step inversion approach (Fig. 8b). Phase velocities are computed at each grid location using Saito (1988) from a model that includes shallow velocity inhomogeneities, different Moho depths, and two domains of a fast and slower upper mantle in accordance with results from real data. Note that this test does not focus on lateral resolution since no tomographical inversion is included. Therefore, it is not surprising that shapes of velocity anomalies are well recovered in Fig. 8(b). However, also amplitudes of anomalies are well resolved in most parts of the crust. The amplitudes of high velocity anomalies at very shallow depths are only slightly overestimated by about 0.05 km s^{-1}. In the upper mantle the relative variation of velocities is well resolved; however, absolute velocities are a bit underestimated by a value close to the upper bound of the model uncertainty of 0.05 km s^{-1}.

When inverting observations of surface wave velocities alone without using independent constraints for the interface depths, trade-offs in the model space are unavoidable. This may be the case for example in the crustal velocity structure. In particular in the northeastern part, high velocities in the upper crust seem to coincide with a slower lower crust (Fig. 7a and c). This trade-off might be related to the depth location of the interface between Layer 1 and 2 and may also explain why shallow high-velocity anomalies are overestimated in the synthetic test. Furthermore, structures with low mantle velocity below a shallow Moho have surface wave dispersion curves that are similar to structures with higher mantle velocities below deeper Moho. The lateral variation that we observe in our study area partly follows this trend in the South, for example from the Oslo Graben to the Caledonian nappes (Fig. 7d, f, g and h). In order to assess the impact of trade-offs between interface depths and velocities, we perform two additional inversion runs fixing the depth of one interface. The difference between these models and the previous one will give us an idea about possible biases related to depth trade-offs.

Figs 9(a)–(c) presents the results of the inversion when bottom of Layer 1 is fixed at 7.5 km depth at all locations. No significant changes are obtained (compare with Figs 7a–c). The general trend in variation of crustal thickness (Fig. 7f) and the averaged Moho depth of about 39 km are consistent with observations made by

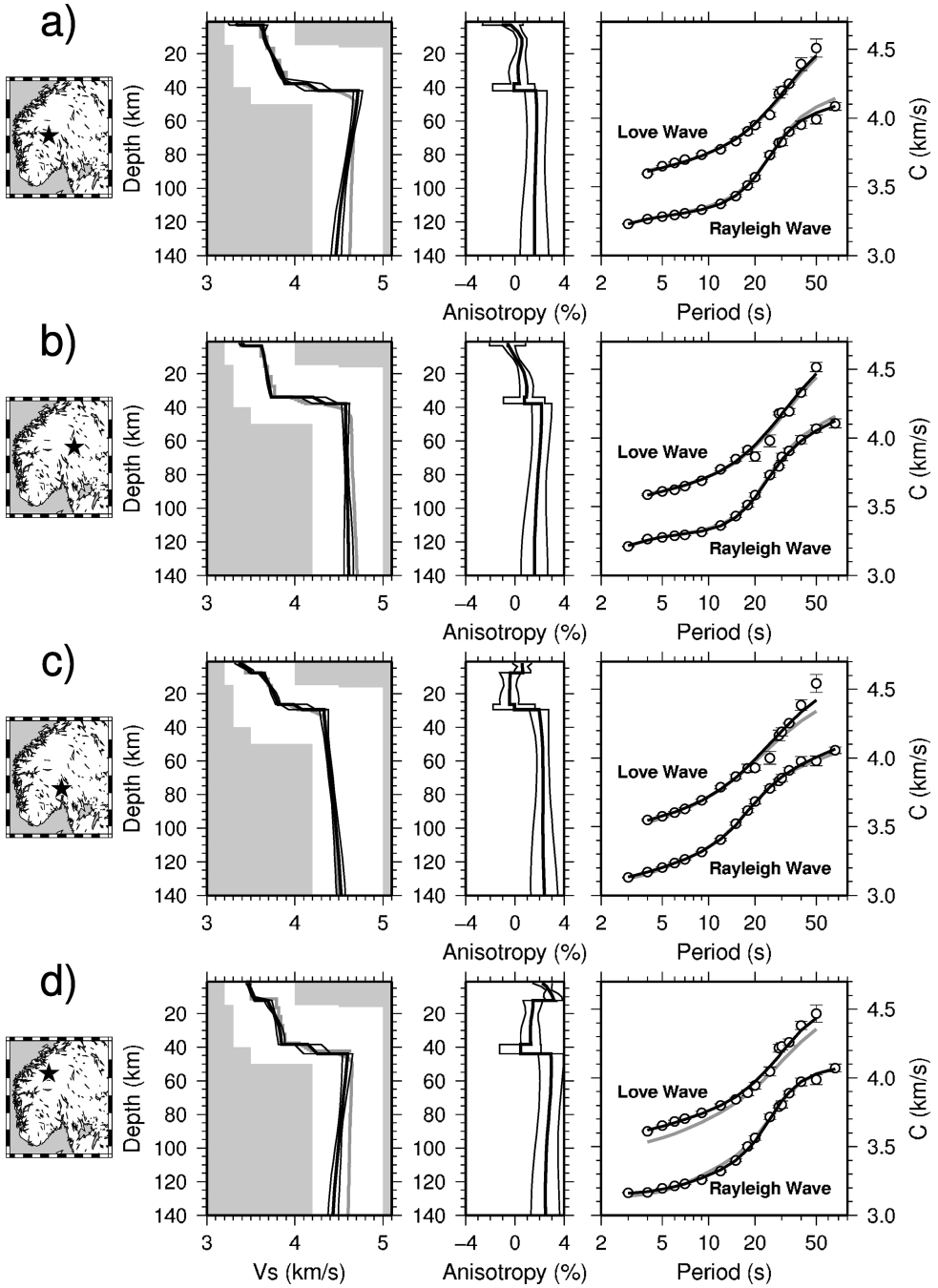

Figure 6. Representative examples of inverted models, Inversion II: Star in leftmost panel indicates location. Light grey profile is initial model obtained from Inversion I. Black profile for V_S (V_{SV}) and radial anisotropy shows final model. Thin black lines indicate *posterior* model standard deviation. Rightmost panels: Symbols show measured phase velocities, grey line dispersion curve of initial model, and black line fit of final model.

previous studies (Stratford *et al.* 2009; Frassetto, in preparation). By inverting with a flat Moho fixed at 39 km (Figs 9d,e and f), the low velocities below the Oslo Graben is a most coherent anomaly that is robust to this numerical experiment. It is also interesting to note that fixing the interfaces to the same depth at all locations has no effect on the upper mantle velocities at depths larger than about 100 km (Fig. 9e), consistent with previous observations by Weidle & Maupin (2008). It is therefore unlikely that variation in velocity structure and interface depths are the sole result of trade-offs, in particular between crustal thickness and shallow mantle structure.

4.3 Radial anisotropy

The inverted ξ value is transformed to relative difference between *SV* and SH wave velocities and plotted in Fig. 10 over different depth ranges. We obtain clear positive anisotropy ($V_{SH} > V_{SV}$) of 2 to 3 per cent within the upper and middle crust in a well-confined area in the northwest. There is also weaker radial anisotropy in the West and in the area of the Oslo Graben, but not larger than 1.5 per cent. The lower crust seems to be rather isotropic since values scatter around zero within the range of the model uncertainty

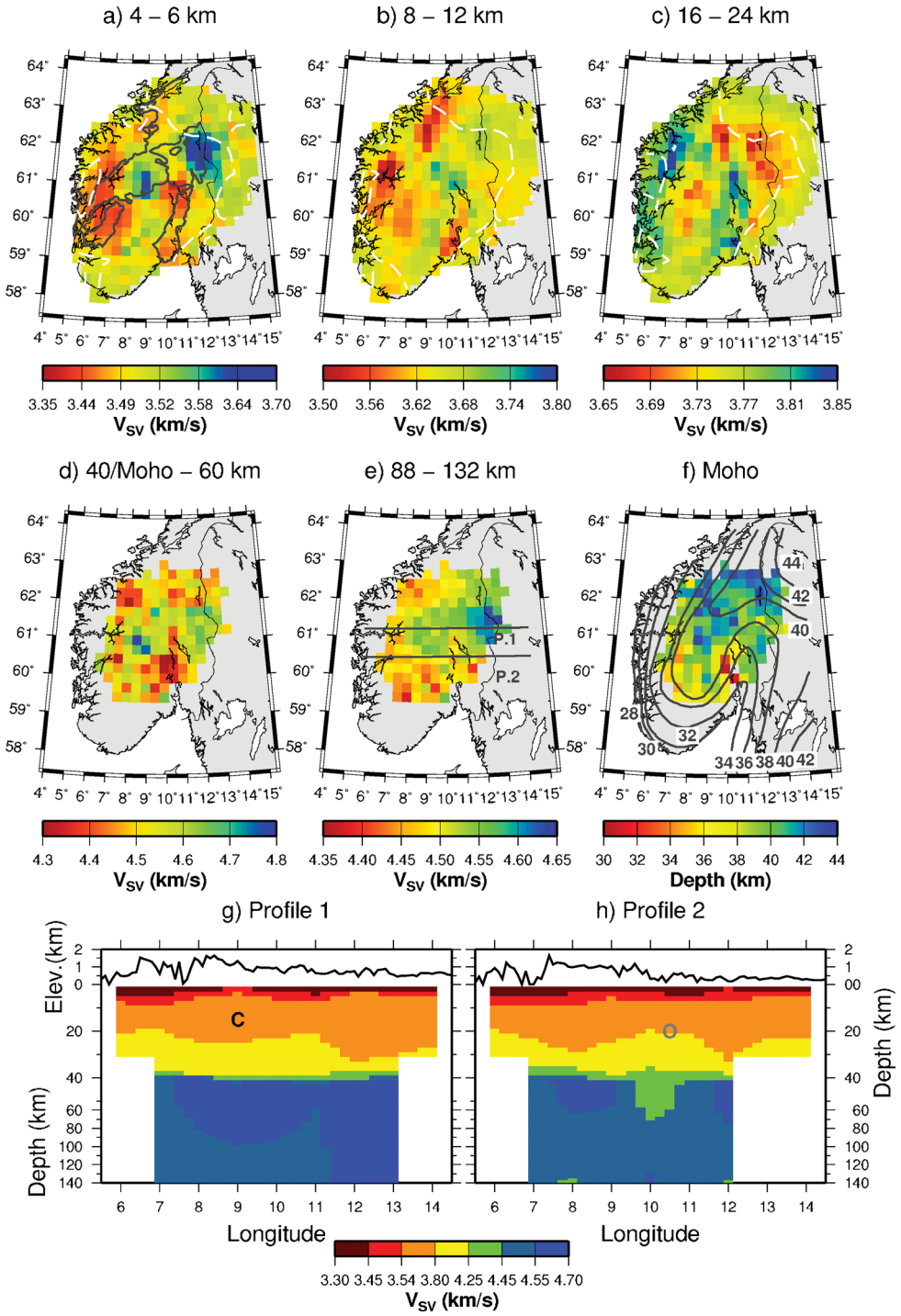

Figure 7. Final inverted V_{SV} model. (a)–(f) Velocities averaged in different depth ranges are shown. If Moho is deeper than 40 km, Moho itself is used in (d) as upper limit. White dashed lines in (a)–(c) are 23 km contours for noise tomography resolution as in Fig. 2 for periods 4 s (a), 9 s (b), and 15 s (c). At larger depths, only locations with reliable phase velocity measurements at longer periods are shown (relative sampling for phase interpolation method >3). Solid lines in (a) is outline of geological units (see Fig. 1). Contours and labels in (f) present Moho depth in km after Stratford *et al.* (2009). Location of profiles in (g) and (h) are shown in (e). Topography (elevation) along profiles is shown. 'C' stands for Caledonides and 'O' for location of Oslo Graben.

of about 1 per cent (see example profiles in Fig. 6), except for a small region in the southwest with a maximum of about 4 per cent. Negative anisotropy in the central part (about −1 per cent) could be a compensation effect of the inversion due to stronger positive anisotropy below the Moho of about 3 per cent. On average the upper mantle shows radial anisotropy of about 2 per cent. Considering the model uncertainty in the upper mantle and the possible trade-off with the lower crust, lateral variations are not very significant. However, overall a weak positive anisotropy in the upper mantle seems to be required to explain Rayleigh and Love waves as indicated by reduced misfit at periods larger than 30 s (Figs 4 and 6), a general observation made also by e.g. Weidle & Maupin (2008).

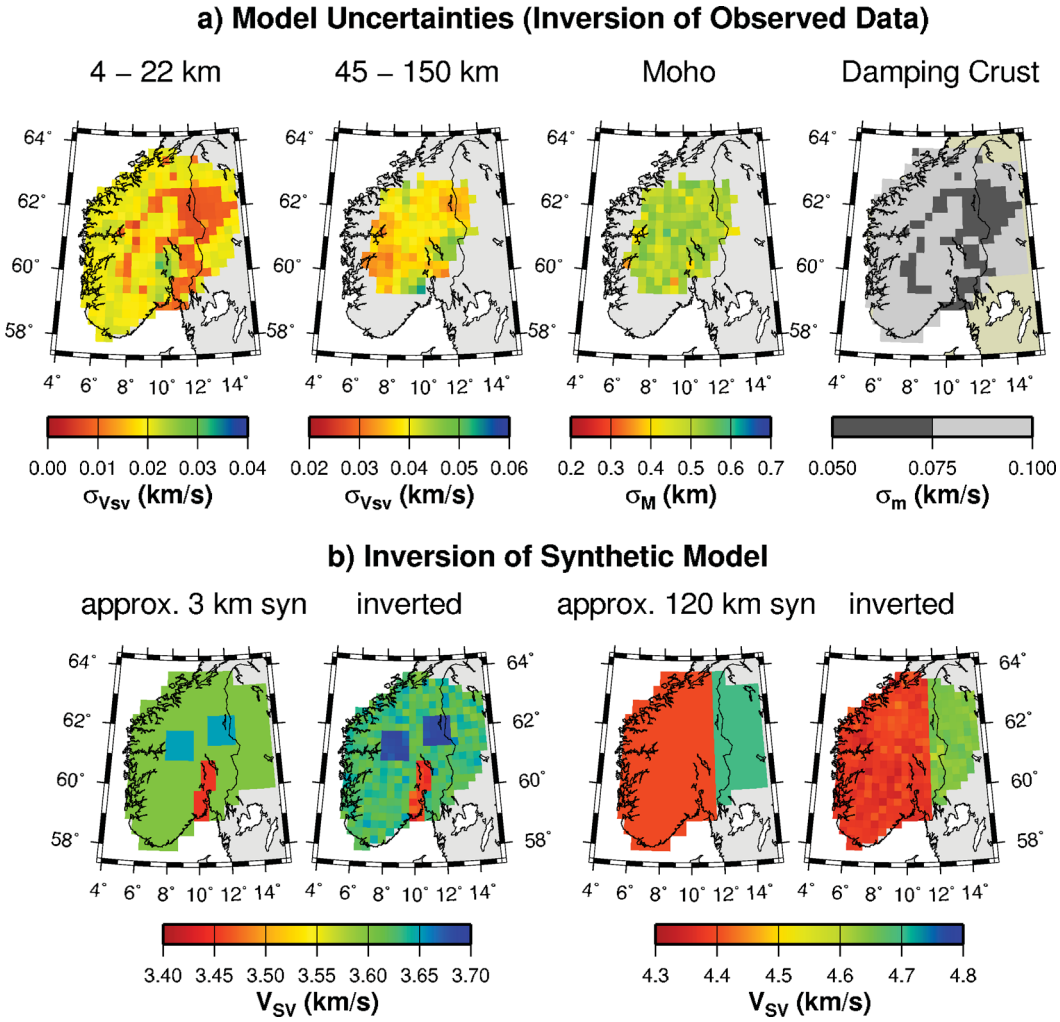

Figure 8. Resolution and uncertainty of inverted model. (a) Standard deviation of V_{SV} is averaged in two depth ranges. Standard deviation of Moho depth is obtained from averaging the ensemble of best fitting models after Inversion I. Rightmost panel shows *a priori* standard deviation (σ_m, damping). Damping is manually increased at some locations by setting σ_m to 0.05. (b) Inversion of synthetic data generated from a model which includes lateral velocity variation. 'Syn' refers to synthetic model and 'inverted' indicates results of inversion.

5 DISCUSSION

Geologically, southern Norway belongs to the Southwest Scandinavian domain, the youngest part of the Fennoscandian shield, consisting mainly of plutonic and metamorphic basement rocks (Stratford & Thybo 2011, and references therein). It was partly reworked during the Caledonian orogeny (440–410 Ma), the latest major orogenic event in the region. The major remnants of the Caledonian orogeny are the nappes overlaying the Fennoscandian basement rocks in the central (e.g. Jotun Nappes) and northeastern part of southern Norway (e.g. Hedmark group) and the highly-metamorphic Western Gneiss Region to the Northwest (Fig. 1). The Oslo Graben is a younger tectonic structure which was formed during Permian rifting (300–240 Ma).

5.1 Crustal structures

On average, the depth distribution of crustal shear wave velocities inverted in this study follows those obtained by active source seismic refraction experiments on three lines in southern Norway (Stratford & Thybo 2011). Furthermore, though surface wave inversion is less sensitive to V_P and densities, Inversion I finds realistic values in accordance with previous studies, i.e. *P*-wave velocities of about 5.7 km s^{-1} in the uppermost crust, 6.6 km s^{-1} in the lower crust, and 8.2 km s^{-1} in the uppermost mantle on average. We obtain crustal densities of about 2.8 g ccm^{-1} on average.

As expected for a region like southern Norway lacking extended, young sedimentary basins onshore, lateral velocity variations in the upper crust at about 5 km depth are rather small (Fig. 7a). We find realistic values for basement rock velocities of about 3.5 km s^{-1}. High density, mafic rocks have been reported at the surface in the Jotun nappes and rather low densities (sedimentary and volcanic rocks) inside the Oslo Graben (Olesen *et al.* 2010). Both observations fit well with the shear wave velocity anomalies found in our study at shallow depths. In particular, the lowest shear wave velocities are found inside the Oslo Graben as well as a bit outside to the west of the northernmost part of the rift, what can both be explained by the presence of sedimentary, low-density rocks (see fig. 7a in Olesen *et al.* 2010). Furthermore, the velocity contrast at shallow depths between the northern part of the Caledonian nappes and the Western Gneiss Region, the lower velocities between the Jotun Nappes to the North and basement rocks to the South, as

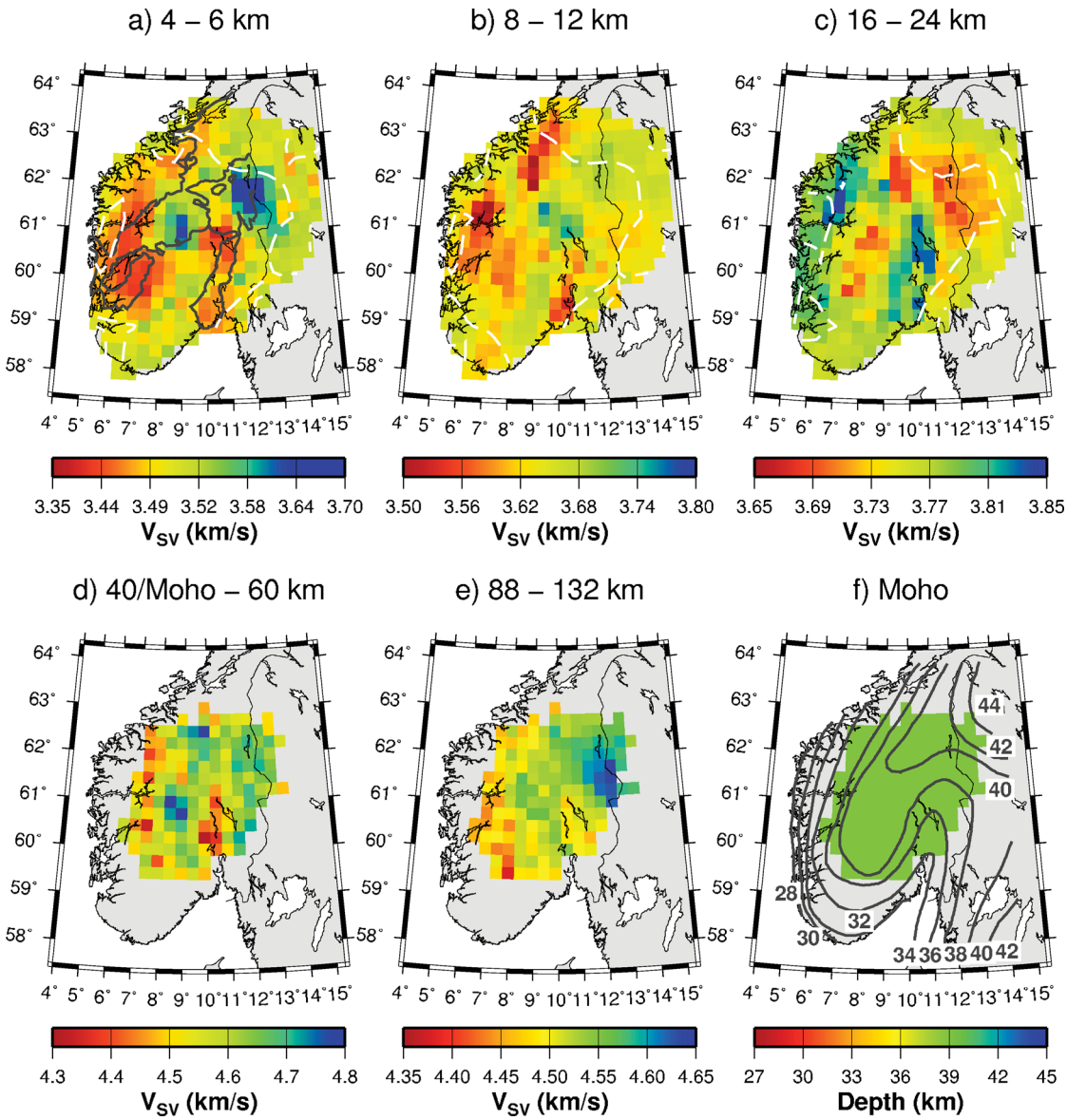

Figure 9. Same as Fig. 7, but using a fixed interface depth between Layer 1 and 2 of 7.5 km (a)–(c) and a fixed Moho depth of 39 km (d)–(f).

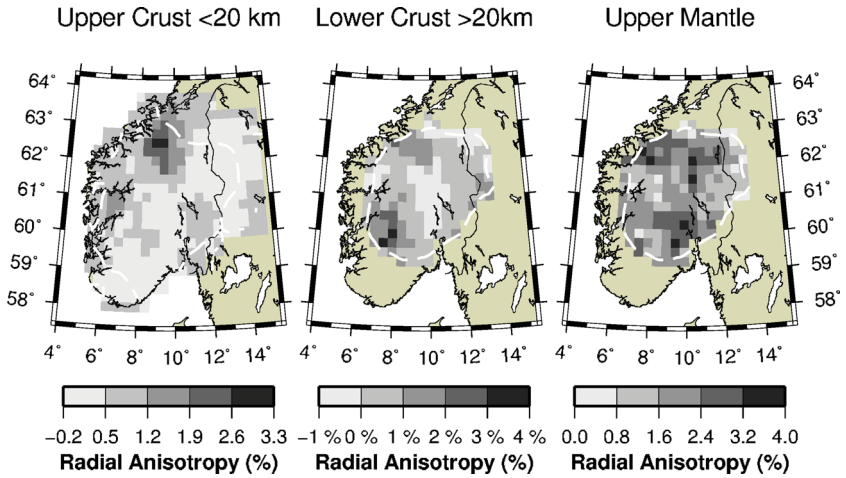

Figure 10. Difference between V_{SH} and V_{SV} (radial anisotropy) in percent with respect to mean of both velocities, averaged in different depth ranges. White dashed contour lines are resolution limits: 23 km resolution of noise tomography at 9 s for upper crust and $S > 3$ (earthquake data) for lower crust and mantle.

well as (in parts) the low velocities along the West coast follow the variation in average surface rock density as reported by Olesen *et al.* (2010). Similar trends of shear wave velocity variations have been found in the Caledonian nappes, inside the Oslo Graben, and to the West of southern Norway by Stratford & Thybo (2011) along the three seismic refraction profiles.

We also find anomalies which cannot be directly related to changing rock densities at the surface and which have not been sampled by the refraction experiment. In contrast to the comparably low densities of the sedimentary rocks of the Hedmark group to the East (11–13 degree E, 61-63 degree N), we find rather high shear wave velocities in the corresponding area (see Fig. 7a). This apparent contradiction between surface geology and observed velocities could be related to the presence of rather high-density rocks (Caledonides, basement rocks) below the sedimentary rocks, maybe including mafic intrusives (Nystuen 1987) and basic rocks which could be related to gravity anomalies further North (Pascal *et al.* 2007). In fact, the profile in Fig. 7(g) shows a low-velocity layer between 12 and 13 degree E which is rather thin compared to areas to the West, leading to higher averaged velocities in the depth range used in Fig. 7(a).

At about 20 km depth, higher velocities of about 3.85 km s^{-1} inside the Oslo Graben (Fig. 7c) can be explained by intrusions due to the Permian volcanism and have also been reported by Stratford & Thybo (2011). Furthermore, evidences have been found for thickening of a fast (high V_P) lower crustal body in the East of the study area (Pascal *et al.* 2007; Stratford & Thybo 2011; Ebbing *et al.* 2012). The transition was found to be rather localized along a line following the Oslo Graben from South to the North, and then bending to Northwest. We do not find clear indications for this observation in our results which is probably due to the fact that surface waves are not sensitive enough to resolve interface depths or thin layers as discussed above. Nevertheless, Fig. 7(c) shows that the zone of higher velocities in the Oslo Graben at about 10.5 degree E and between 59 and 61 degree N seems to continue in the lower crust at about 20 km depth towards Northwest (8 degree E, 62 degree N), which correlates well with the suggested location of the transition from a thin to a thick fast lower crustal body.

Inversion of synthetic models also showed that a fast lower crustal body may result in an underestimation of the Moho depth (not shown in Fig. 8). However, as shown in Fig. 7(f), Moho variations are consistent with results from active source seismic refraction profiles in southern Norway (Stratford *et al.* 2009). In particular, we find the same offset between highest surface topography and deepest Moho along the profiles from West to East (Fig. 7h), a thinning of the crust underneath the Oslo rift (Fig. 7h), and a general trend of crustal thickening towards North-East (Fig. 7f). Our results however suggest that the crustal thinning in the Oslo Graben is slightly shifted to the West compared to Stratford *et al.* (2009). Towards East across the Swedish border, receiver functions revealed lack of strong impedance contrasts what indicates a weak or gradient-like Moho (Frassetto, in preparation). Therefore, crustal thickness in the East may not be well constrained which could also have an effect on our results since our parameterization favours a strong contrast between crust and mantle.

We find two regions of pronounced, positive crustal radial anisotropy (Fig. 10). Along the eastern part of the anisotropic area in the Northwest in the upper and middle crust (<20 km depth), anomalous high velocities have been found at shallow depths by different active seismic source experiments (Stratford & Thybo 2011). The depth structure was however not well constrained. The presence of high-density rocks related to the Caledonian nappes was suggested to explain the observation of high velocities. Outcrops of olivine-rich dunites are found to the west of the anisotropic area (Neeb 2006). If present further east deeper in the crust, and if deformed for example during the Caledonian orogeny, dunites could cause both anisotropy and high velocities.

Middle to lower-crustal radial anisotropy in the Western United States has been found recently using ambient noise in areas which have undergone significant extension and which could therefore show preferred orientation of anisotropic minerals (Moschetti *et al.* 2010b,a). Similar observations have been made in Tibet based on earthquake generated surface wave data (Shapiro *et al.* 2004) and ambient noise (Guo *et al.* 2012). The northwesternmost part of the Western Gneiss region in southern Norway has undergone extensional, post-caledonian faulting along the Møre-Trøndelag fault complex (Gabrielsen *et al.* 1999), which could have resulted in frozen-in anisotropy. Macroscopic anisotropy also results from heterogeneities but very strong contrasts of ±50 per cent are required to produce moderate anisotropy (Capdeville *et al.* 2010) and it is very unlikely that such contrasts are present in the crust in southern Norway.

5.2 Uppermost mantle structures

Figs 7(e), (g) and (h) reveal lateral variation in uppermost mantle shear wave velocities. Sub-Moho variations are a bit stronger (4.3 to 4.8 km s^{-1}) compared to results from seismic refraction (4.65 to 4.7 km s^{-1}, Stratford & Thybo 2011), particularly considering the low velocity anomaly in the Oslo Graben area.

The velocity contrast between the western and eastern part of the northern cross-sections (Profile 1) at depths of about 100 km, which is a robust result using different Moho depths (Fig. 9e), shows a clear transition between two different upper mantle domains. An averaged model of southern Norway inverted from long-period Rayleigh waves (Maupin 2011) has shown that the upper mantle between 100 and 200 km depth has a character of a young continental platform with shear wave velocities of about 4.4 km s^{-1} in agreement with observation in Denmark to the South, rather than being a shield-like upper mantle with velocities between 4.6 and 4.8 km s^{-1} as observed in southern Sweden (Cotte *et al.* 2002) or other cratonic areas. With our model we are able to confirm those (1-D) results and to locate the transition between the shield mantle to the East and the slower upper mantle to the West. The location of the rather sharp transition in upper mantle structure was also recently revealed by *P*- and *S*-wave tomography (Medhus *et al.* 2012; Wawerzinek *et al.* 2012). The anomalously slow mantle underneath southern Norway was found to persist down to at least 400 km, though amplitudes and extent differ between the different studies.

By integrating results for *P*- and *S*-wave velocities from Medhus *et al.* (2012) and Maupin (2011) as well as gravity data into a self-consistent modelling approach which takes into account thermal and compositional effects, Gradmann *et al.* (in preparation) showed that a major change in lithospheric thickness, and thus temperature, from 100 to 200 km is required to explain the observed velocity contrast between southern Norway and Sweden. This step in the lithosphere is thought to be a result of old tectonic events (at least Proterozoic). Pascal & Olesen (2009) pointed out that dynamic topography due to a warm upper mantle alone is not able to explain the recent elevation of the Scandes. A relation between the revealed mantle anomaly and the uplift processes most likely exists, but has to be investigated and discussed in more detail in ongoing studies.

6 CONCLUSIONS

We presented a 3-D shear wave model for southern Norway inverted from Rayleigh and Love wave phase velocity observations. The use of ambient seismic noise as well as earthquake records allowed for a depth resolution suitable for imaging shallow crustal to uppermost mantle structures. We have inverted phase velocity maps for local velocity depth profiles using a direct search and subsequently a linear inversion technique. Results have been found to be consistent with recent seismic and gravity studies in most parts. Crustal velocity variations are rather small and follow mainly surface geology, i.e. rock densities. Findings for crustal thickness confirm lateral Moho depth variations in the area found by controlled source seismic refraction and receiver functions. Furthermore, we found clear indications for local crustal radial anisotropy, which explains observed Rayleigh-Love wave discrepancy. Our 3-D shear wave model confirms the presence of two upper mantle domains. We were able to localize the transition from a slow to fast uppermost mantle between southern Norway and western Sweden.

Our model will benefit from integration of other seismic data sets to compensate the limited resolution of surface wave inversion to constrain interface depths and thin layers. An ongoing study will include receiver functions for a joint inversion with phase velocity observations to further improve the shear wave velocity depth model of southern Norway.

ACKNOWLEDGMENTS

MAGNUS waveforms were recorded with the mobile KArlsruhe Broadband Array of the Karlsruhe Institute of Technology (KIT), Germany as well as with permanent stations of the NORSAR array, the Norwegian National Seismological Network and GSN. Continuous data from the NORSAR array were kindly provided by Johannes Schweitzer. We thank Andy Frassetto for providing us with the DANSEIS data (University of Copenhagen). Financial support for the MAGNUS experiment was provided by the Universities of Aarhus, Copenhagen, Karlsruhe and Oslo as well as NORSAR. This work has been done in the framework of the ESF EUROCORES TOPO-EUROPE Program 07-TOPO-EUROPE-FP-014. We acknowledge financial support from the Research Council of Norway. Figures have been prepared using the Generic Mapping tools (Wessel & Smith 1998). We appreciate the constructive comments and suggestions of both anonymous reviewers.

REFERENCES

Barmin, M., Ritzwoller, M. & Levshin, A., 2001. A fast and reliable method for surface wave tomography, *Pure appl. Geophys.,* **158**(8), 1351–1375.

Bensen, G., Ritzwoller, M., Barmin, M., Levshin, A., Lin, F., Moschetti, M., Shapiro, N. & Yang, Y., 2007. Processing seismic ambient noise data to obtain reliable broad-band surface wave dispersion measurements, *Geophys. J. Int.,* **169**(3), 1239–1260.

Capdeville, Y., Guillot, L. & Marigo, J., 2010. 2-d non-periodic homogenization to upscale elastic media for P–SV waves, *Geophys. J. Int.,* **182**(2), 903–922.

Chalmers, J., Green, P., Japsen, P. & Rasmussen, E., 2010. The scandinavian mountains have not persisted since the Caledonian orogeny. a comment on Nielsen *et al.* (2009a), *J. Geodyn.,* **50**(2), 94–101.

Cotte, N., Pedersen, H. & TOR Working Group, 2002. Sharp contrast in lithospheric structure across the Sorgenfrei-Tornquist Zone as inferred by Rayleigh wave analysis of TOR1 project data, *Tectonophysics,* **360**(1-4), 75–88.

Ebbing, J., England, R., Korja, T., Lauritsen, T., Olesen, O., Stratford, W., & Weidle, C., 2012. Structure of the scandes lithosphere from surface to depth, *Tectonophysics,* **536–537**(1-4), 1–24.

Ebbing, J. & Olesen, O., 2005. The Northern and Southern Scandes–structural differences revealed by an analysis of gravity anomalies, the geoid and regional isostasy, *Tectonophysics,* **411**(1-4), 73–87.

Gabrielsen, R., Odinsen, T. & Grunnaleite, I., 1999. Structuring of the Northern Viking Graben and the Møre Basin; the influence of basement structural grain, and the particular role of the Møre-Trøndelag Fault Complex, *Mar. Petrol. Geol.,* **16**(5), 443–465.

Guo, Z., Gao, X., Wang, W. & Yao, Z., 2012. Upper- and mid-crustal radial anisotropy beneath the central Himalaya and southern Tibet from seismic ambient noise tomography, *Geophys. J. Int.,* **189**(2), 1169–1182.

Japsen, P. & Chalmers, J., 2000. Neogene uplift and tectonics around the North Atlantic: overview, *Global Planet. Change,* **24**(3-4), 165–173.

Köhler, A., Weidle, C. & Maupin, V., 2011. Directionality analysis and Rayleigh wave tomography of ambient seismic noise in southern Norway, *Geophys. J. Int.,* **184,** 287–300.

Köhler, A., Weidle, C. & Maupin, V., 2012. On the effect of topography on surface wave propagation in the ambient noise frequency range, *J. Seismol.,* **16,** 221–231.

Lacoss, R., Kelly, E. & Toksoz, M., 1969. Estimation of seismic noise structure using arrays, *Geophysics,* **34**(1), 21–36.

Levshin, A., Yanovskaya, T., Lander, A., Bukchin, B., Barmin, M., Ratnikova, L. & Its, E., 1989. *Seismic Surface Waves in a Laterally Inhomogeneous Earth*, ed. Keilis-Borok, V.I., Kluwer, Norwell, MA.

Lundin, E. & Doré, A., 2002. Mid-cenozoic post-breakup deformation in the "passive" margins bordering the Norwegian-Greenland Sea, *Mar. Petrol. Geol.,* **19**(1), 79–93.

Maupin, V., 2011. Upper-mantle structure in southern Norway from beamforming of Rayleigh wave data presenting multipathing, *Geophys. J. Int.,* **185,** 985–1002.

Medhus, A., Balling, N., Jacobsen, B., Weidle, C., England, R., Kind, R., Thybo, H. & Voss, P., 2012. Upper-mantle structure beneath the Southern Scandes Mountains and the Northern Tornquist Zone revealed by P-wave traveltime tomography, *Geophys. J. Int.,* **189**(3), 1315–1334.

Moschetti, M., Ritzwoller, M., Lin, F. & Yang, Y., 2010a. Crustal shear wave velocity structure of the western United States inferred from ambient seismic noise and earthquake data, *J. geophys. Res.,* **115**(B10), B10306, doi:10.1029/2010JB007448.

Moschetti, M., Ritzwoller, M., Lin, F. & Yang, Y., 2010b. Seismic evidence for widespread western-US deep-crustal deformation caused by extension, *Nature,* **464**(7290), 885–889.

Neeb, P., 2006. Mineral resources in Norway: the Norwegian mining and quarrying industry in 2005, *NGU report,* 048.

Nielsen, S. *et al.*, 2009. The evolution of western Scandinavian topography: a review of Neogene uplift versus the ICE (isostasy-climate-erosion) hypothesis, *J. Geodyn.,* **47**(2–3), 72–95.

Nystuen, J., 1987. Synthesis of the tectonic and sedimentological evolution of the late Proterozoic-early Cambrian Hedmark Basin, the Caledonian Thrust Belt, southern Norway, *Norsk geologisk tidsskrift,* **67**(4), 395–418.

Olesen, O. *et al.*, 2010. New aeromagnetic and gravity compilations from Norway and adjacent areas: methods and applications, in *Petroleum Geology: From mature basins to new frontiers.* Proc. 7th Petrol. Geol. Conf., vol. 7, pp. 559–586.

Pascal, C., Ebbing, J. & Skilbrei, J., 2007. Interplay between the Scandes and the Transscandinavian Igneous belt: integrated thermal and potential field modelling of the Central Scandes profile, *Norwegian J. Geol.,* **87,** 3–12.

Pascal, C. & Olesen, O., 2009. Are the Norwegian mountains compensated by a mantle thermal anomaly at depth?, *Tectonophysics,* **475**(1), 160–168.

Ritzwoller, M. & Levshin, A., 1998. Eurasian surface wave tomography: group velocities, *J. geophys. Res.,* **103,** 4839–4878.

Rohrman, M. & van der Beek, P., 1996. Cenozoic postrift domal uplift of North Atlantic margins: an asthenospheric diapirism model, *Geology,* **24**(10), 901–904.

Sabra, K., Gerstoft, P., Roux, P., Kuperman, W. & Fehler, M., 2005. Extracting time-domain Green's function estimates from ambient seismic noise, *Geophys. Res. Lett.,* **32,** L03310, doi:10.1029/2004GL021862.

Saito, M., 1988. Disper80: a subroutine package for the calculation of seismic normal-mode solutions, *Seismol. Algorithms*, pp. 293–319.

Sambridge, M., 1999. Geophysical inversion with a neighbourhood algorithm–I. searching a parameter space, *Geophys. J. Int.,* **138**(2), 479–494.

Shapiro, N. & Campillo, M., 2004. Emergence of broadband Rayleigh waves from correlations of the ambient seismic noise, *Geophys. Res. Lett.,* **31**(7), 1615–1619.

Shapiro, N., Ritzwoller, M., Molnar, P. & Levin, V., 2004. Thinning and flow of Tibetan crust constrained by seismic anisotropy, *Science,* **305**(5681), 233–236.

Stratford, W. & Thybo, H., 2011. Seismic structure and composition of the crust beneath the southern Scandes, Norway, *Tectonophysics,* **502**(3–4), 364–382.

Stratford, W., Thybo, H., Faleide, J., Olesen, O. & Tryggvason, A., 2009. New Moho Map for onshore southern Norway, *Geophys. J. Int.,* **178**(3), 1755–1765.

Tarantola, A. & Valette, B., 1982. Generalized nonlinear inverse problems solved using the least squares criterion, *Rev. Geophys. Space Phys.,* **20**(2), 219–232.

Wathelet, M., 2008. An improved neighborhood algorithm: parameter conditions and dynamic scaling, *Geophys. Res. Lett.,* **35**(9), L09301, doi:10.1029/2008GL033256.

Wathelet, M., Jongmans, D. & Ohrnberger, M., 2004. Surface wave inversion using a direct search algorithm and its application to ambient vibration measurements, *Near Surface Geophys.,* **2**(4), 211–221.

Wawerzinek, B., Joachim, R.R., Ritter, J. & Roy, C., 2012. New constraints on the 3-D shear wave velocity structure of the upper mantle underneath Southern Scandinavia revealed from non-linear tomography, *Tectonophysics*, submitted.

Weidle, C., 2012. Surface wave phase velocity maps from multiscale wave field interpolation, *Computational Geosci.,* **16**(3), 535–549.

Weidle, C. & Maupin, V., 2008. An upper-mantle S-wave velocity model for Northern Europe from Love and Rayleigh group velocities, *Geophys. J. Int.,* **175**(3), 1154–1168.

Weidle, C. *et al.*, 2010. MAGNUS–A seismological broadband experiment to resolve crustal and upper mantle structure beneath the southern Scandes mountains in Norway, *Seism. Res. Lett.,* **81**(1), 76–84.

Wessel, P. & Smith, W., 1998. New improved version of GMT released, *EOS, Trans. Am. geophys. Un.,* **79,** 579, doi:10.1029/98EO00426.

Yang, Y., Shen, W. & Ritzwoller, M., 2011. Surface wave tomography on a large-scale seismic array combining ambient noise and teleseismic earthquake data, *Earthq. Sci.,* **24**(1), 55–64.

Yao, H., Beghein, C. & Van Der Hilst, R., 2008. Surface wave array tomography in SE Tibet from ambient seismic noise and two-station analysis–II. Crustal and upper-mantle structure, *Geophys. J. Int.,* **s173**(1), 205–219.

SUPPORTING INFORMATION

Additional Supporting Information may be found in the online version of this article:

Figure S1. Rayleigh wave phase velocity dispersion curves for four station pairs obtained by time frequency analysis. Locations of receivers and corresponding noise cross-correlation functions (20-month stacks, scale is in seconds) are shown. Thick black line indicates dispersion curve averaged over all 3-month stacks. Thin lines show standard deviation. Colored lines represent dispersion curve obtained from cross-correlation stacks over entire record (red), over summer months (green, June to August), and over winter months (blue, November to January), respectively.

Figure S2. Same as Fig. S1 for Love waves.

Figure S3. Rayleigh and Love wave phase velocity maps at selected periods obtained by phase interpolation of earthquake observations using MAGNUS data only. White dashed lines indicate resolution limits: relative sampling contour of three (number of velocity estimates by number of nodes).

Please note: Wiley-Blackwell are not responsible for the content or functionality of any supporting materials supplied by the authors. Any queries (other than missing material) should be directed to the corresponding author for the article.